EUROPEAN ORGANIZATION FOR NUCLEAR RESEARCH

CERN ISR-MA/71-29

FLUENCE AND DOSE MEASUREMENTS WITH ACTIVATION AND SPALLATION DETECTORS NEAR INTERNAL TARGETS AT THE CERN PROTON SYNCHROTRON

by

Jorma T. Routti and M.H. Van de Voorde
ISR Division
and
M. Höfert
Health Physics

Geneva, Switzerland
June 29, 1971

ABSTRACT

A series of measurements have been performed at the CERN Proton Synchrotron to study the doses and particle fluences near thick internal targets. Conventional activation detectors and high-threshold spallation detectors as well as directly reading dosimeters were used. The effect of local shielding on low- and high-energy particle fluxes is studied downstream from targets. A detailed study of a multitude of spallation reactions induced in copper is used to evaluate particle fluxes above different threshold energies and to unfold the energy spectra of high-energy particles. The experimental results with flux and dose meters are used to determine practical fluence-to-dose conversion factors.

C O N T E N T S

ABSTRACT

1. INTRODUCTION 1

2. FLUX AND DOSE METERS USED 2

2.1 Conventional activation detectors
2.2 Spallation detectors
2.3 Phosphate glass dosimeter

3. IRRADIATIONS AT THE CERN PROTON SYNCHROTRON 5

4. EXPERIMENTAL RESULTS 6

4.1 Low- and high-energy particle fluences
4.2 Results with spallation detectors
4.3 Results with phosphate glass dosimeters

5. FLUENCE-TO-DOSE CONVERSIONS 12

6. CONCLUSIONS 16

ACKNOWLEDGEMENTS 18

REFERENCES 19

TABLES 21

FIGURES 34

1. INTRODUCTION

In this paper we report the results and conclusions of a series of experiments performed at the CERN Proton Synchrotron. The radiation fields near thick internal targets were studied by using activation detectors, both of conventional types and high-threshold spallation detectors, and directly reading dosimeters. The detectors used are described in section 2. In the irradiations several beam energies, target materials, and local shields were used, as described in section 3. The experimental results on doses and low- and high-energy particle fluences as well as detailed study of the spallation detectors are presented in section 4. The comparison of directly reading dosimeters with the activation detector results enables us to derive practical fluence-to-dose conversion factors applicable to the experimental conditions used, as discussed in section 5.

In the fluence-to-dose conversions we use the colouration of phosphate glass as reference dosimeter. In the same irradiations a number of other dosimeters were used and compared to the readings of the phosphate glass. An intercomparison of the various dosimeters as well as a discussion of energy and target dependence of the readings and of the effect of local shielding has been presented in an earlier report[1)].

2. FLUX AND DOSE METERS USED

2.1 Conventional activation detectors

Several activation detectors based on the measurement of radioactivity induced through nuclear reactions by charged and neutral particles were employed. The measured activity or disintegration rate of such a detector, after an irradiation in a time-independent radiation field, is expressed as

$$A = N\, g \left(1-\exp\left(-\frac{\ell n 2\; t_i}{t_{1/2}}\right)\right)\exp\left(-\frac{\ell n 2\; t_w}{t_{1/2}}\right)\int_{E_{min}}^{E_{max}} \sigma(E)\, \varphi(E)dE \quad (1\,a)$$

$$= c \int_{E_{min}}^{E_{max}} \sigma(E)\, \varphi(E)dE \quad (1\,b)$$

$$= c\, \sigma_{eff} \int_{E_{threshold}}^{E_{max}} \varphi(E)dE \quad (1\,c)$$

$$= c\, \sigma_{eff}\, F_{threshold} \quad (1\,d)$$

$$\text{where } \sigma_{eff} = \frac{\int_{E_{threshold}}^{E_{max}} \sigma(E)\, \varphi(E)dE}{\int_{E_{threshold}}^{E_{max}} \varphi(E)dE} \quad . \quad (1\,e)$$

In the above equations A is the measured disintegration rate, N is the number of target nuclei in the detector, assumed to be constant, g is an efficiency factor taking into account the counter efficiency and the fraction of the decays counted, $t_{1/2}$ is the half life of the induced activity, t_i is the irradiation time, t_w is the waiting time following the irradiation, $\sigma(E)$ is the cross section of the activation reaction, $\varphi(E)$ is the flux spectrum of the inducing particles, and E_{min} and E_{max} define the energy range of the particle spectrum. The energy dependence and the threshold of the nuclear reaction define a region of sensitivity where the effective cross section σ_{eff}, as definded above, may be used to obtain an

approximate particle flux, $F_{threshold}$, above the threshold of the activation reaction.

Several conventional activation detectors which are routinely used for flux monitoring were employed in the experiments. Detailed description of the experimental techniques have been given elsewhere[2], only a brief summary of the characteristics of the detectors and their cross sections are given in table 1 and figure 1.

2.2 Spallation detectors

The extension of the activation detector techniques to high energies makes it desirable to use nuclear reactions with equally high threshold energies. Such reactions are provided with a wide range of threshold energies by the spallation phenomena. Experimental and mathematical techniques have been developed to measure a multitude of spallation reactions in a single detector and to determine the energy spectrum of the inducing particles from these measurements[3]. As a preliminary phase of more detailed measurements we exposed and analyzed some spallation detectors in these PS experiments.

Spallation reaction is a result of a collision between a high-energy particle and the target nucleus. The mechanism of such a reaction is only approximatively known. The first stage is an intranuclear cascade or fragmentation in which the number of protons and neutrons emitted may be assumed to be proportional to their availability in the target nucleus. This stage is followed by a slower evaporation chain leading from the highly exited intermediate states to the final configuration. A large number of isotopes, lighter than the target nucleus, are thus produced through the high-energy spallation phenomena.

The number of reaction products increases with increasing mass number of the target nuclei. For practical studies we use copper detectors for the following reasons. The number of reaction products is small enough to make it possible through high-resolution gamma-spectroscopic techniques, described later, to distinguish and measure the radioisotopes produced. On the other hand the target nuclei are

heavy enough to yield a large number of isotopes,or threshold reactions, in a single detector. And thirdly the validity of the cross section formalism,discussed next, is best with medium heavy targets, such as copper.

A semi-empirical formula for the spallation cross sections has been described by Rudstam[4]. In his model the existing experimental data was used to determine parameters in an analytical representation of the cross sections. The formalism assumes an exponential yield-mass distribution along the stability line of the chart of nuclides and an approximatively Gaussian charge distribution which is symmetric about this line. This model makes it very convenient to estimate cross sections for various spallation reactions. A computer program written in the course of the earlier work[3] is used to compute the yield cross sections. Figure 2 shows the computed cross sections for producing a number of isotopes from copper.

The radioisotopes produced in the detector material are measured through a careful analysis of the gamma-ray spectra which they emit. The gamma spectra are counted with a high-resolution spectrometer consisting of a Ge(Li) detector and a multichannel analyzer. The spectra accumulated are analyzed with aid of an automatic computer program SAMPO run on the CDC-6000 series computers of CERN. The code performs peak search and integrations by fitting internally calibrated analytical functions to the photopeaks in the spectra. The code also includes complete options for energy and efficiency calibrations needed for absolute determinations of the induced activities. Full description of the mathematical methods and the program has been given elsewhere[5,6].

2.3 Phosphate glass dosimeter

The absorbed radiation energy can be measured in principle with an absolute dosimeter such as a calorimeter. Unfortunately there are no suitable absolute dosimeters available for measurements and calibrations of complex radiation fields found in the vicinity of high-energy accelerators. Instead most dosimeters used are based on measuring secondary radiation effects, such as colouration of glass

or plastic, luminescent phenomena, gas evolution, etc.. In the intercomparison of different dosimeters, which we have described earlier[1], we used as a reference dosimeter a phosphate glass dosimeter. We use this dosimeter to determine practical fluence-to-dose convension factors.

The phosphate glass is composed of P_2O_5 (70.5 % weight), K_2O (12), Al_2O_3 (9), MgO (4), B_2O_3 (3), and various components (1.5). Ionizing radiation causes measurable changes in the optical properties of this glass. The change in percent transmission is measured with a spectrophotometer at 510 nm. The initial fading, which can be as much as 25 % in the first 24 hours, is accelerated by a pre-reading heat treatment at 120°C 10 min. The remaining darkening fades only a few per cent over a period of a month. Exposed glass can be reused as the darkening can be removed by annealing the glass at 480°C[7].

The glass dosimeters have been calibrated by comparing their response to that of chemical dosimeters (Fricke, Ceric-cerous) after an exposure to a high-level ^{60}Co source. Two glass thicknesses, 5 mm and 1.5 mm, cover the dose ranges 10^4 - 5 x 10^5 rad and 2 x 10^5 - 2 x 10^7 rad, respectively.

3. IRRADIATIONS AT THE CERN PROTON SYNCHROTRON

The irradiations were performed at the straight section 47 of the CERN proton synchrotron. Internal targets of dimensions 3 x 4 x 38 (mm) made of Be or Cu were inserted at 43.5 cm downstream from magnet 46. The dosimeters were placed on three plexiglass plates in the 175 cm wide gap between magnets 46 and 47. The effect of local shielding was investigated by placing concrete slabs of 20 cm thickness between the plates in some irradiations, as shown in figure 3. Figure 4 shows the placement of the dosimeters on the plates.

Proton momenta of 12, 19.2, and 24 GeV/c were used in the experiments. The intensity of the accelerated beam varied from 1.0 10^{12} to 1.6 x 10^{12} protons per pulse, the repetition rate of pulses from 1.2 to 2.3 sec, and the total number of pulses per run between 1505 and 1922 pulses. In order to obtain a suitable exposure

for all detectors, some of them were removed after 5 or 200 pulses already. The experimental parameters for different runs are summarized in table 2.

4. EXPERIMENTAL RESULTS

4.1 Low- and high-energy particle fluences

In order to compare and correlate the results from different detectors and runs we first normalize all results to correspond to a circulating beam intensity of 10^{12} protons. The fluences of various activation detectors are given in table 3.

The limited number of positions employed do not permit us to specify detailed angular distributions of the particle fluences in different experiments. We determine average dependence of the readings on the primary particle energy and local shielding. Detailed distributions have been reported earlier both for thin target bombardments[8] and for measurements around a massive beam stopper[9].

The correlations between the results obtained in different runs are summarized in table 4. For instance, the ratio between the fluences measured with detector 2, averaged over the three positions between runs 4 and 1, gives the energy dependence of the epicadmium neutron flux. Similarily the ratios of various particle fluxes are given as a function of target material and local shielding.

It should be noted that the spacial distribution of the radiation field may change significantly between the runs as is evidenced by the readings of the phosphate glass dosimeters placed in more numerous positions, see section 4.3.

The overall energy dependence measured with all activation detectors is in fair agreement with the results obtained with a large number of dosimeters as reported earlier[1]. Ratios 0.64 between 12 and 24 GeV/c, and 0.86 between 19.6 and 24 GeV/c were found, corresponding to an energy dependence of the form, dose = constant x energy $^{0.66}$. No significant difference is noticed between Be and Cu targets, confirming the results measurements with dosimeters[1].

The effect of local shielding is most noticable with low energy particle fluxes which show a significant build-up. With concrete shield of up to 40 cm thickness no significant decrease is measured even with higher threshold detectors. This finding is also in agreement with the earlier results with dosimeters. One may thus conclude that a local shield of up to 40 cm concrete is not efficient in protecting components close to a loss point. Lead shield was found to be of small efficiency in the dosimeter experiments, the reduction after 40 cm of lead was found to be about 50 % in well shielded locations[1].

The increase of low-energy particle fluences with concrete shield is not accompanied by similar increase in the dose levels. Rather the doses stay almost unchanged as do the high-energy particle fluences. We can thus qualitatively conclude that the primary contribution to the doses measured with phosphate glasses comes from the high-energy particles. A quantitative evaluation of the fractions will be given in section 5 where we discuss the fluence-to-dose conversions.

4.2 Results with spallation detectors

In order to study the feasibility of measuring high-energy particle fluxes and their energy spectra by using several spallation reactions induced in a single element we exposed some copper foils in the PS experiments. The following discussion is limited to the analysis of the results obtained with thick foils exposed 48.6 cm downstream from the target, 10 cm away from the vacuum chamber, behind a lead shield of 20 cm. The momentum of the beam hitting the target was 24 GeV/c and the total number of protons accelerated was 2.2×10^{15}. The secondary particle flux produced sufficient activity in foils of about 40 g to measure the induced radioactivities, including those of long half lives.

The exposed foils were counted with a high resolution gamma spectrometer consisting of a 35 cm^3 Ge(Li) semiconductor detector by Ortec and a 4096 channel pulse height analyzer by Laben. A gamma energy range up to 2 MeV was studied in detail.

Figure 5 shows two gamma ray spectra measured after waiting times of 11 and 51 hours. The radioisotopes identified are indicated on these graphs. The initial identification is aided by a graphical compilation of gamma ray spectra[3]. This technique combines in a graphical form the plotted spectra with the decay scheme and detector calibration information, in particular the associative relationships between photopeaks emitted by the same radionuclides. This analysis is complemented by the numerical analysis of the spectra with SAMPO program which yields the energies and intensities of the gamma ray lines with statistical and calibration error estimates[5,6].

The output from SAMPO program is further analyzed by another code which identifies the gamma-ray emitters by using compilations of gamma-ray energies and relative intensities[10,11]. This code also computes the saturation activities of the isotopes identified and lists the possibly interfering isotopes. The results are summarized in detail in table 5.

By using the equation (1d), $A = c\ \sigma_{eff}\ F_{threshold}$, we determine the particle fluxes above different threshold energies. The effective cross sections are approximated by the asymptotic high energy values calculated by using Rudstam's model, similarily the thresholds are defined by this model at the point where the cross sections are 1 % of their peak values. These quantities as well as the computed particle fluxes are given in table 6.

The fluences determined by using the effective cross sections are listed in order of increasing threshold energies. As should be expected they decrease with increasing threshold energies. However, there are some exceptions from monotonous decrease. These indicate uncertainties in the cross sections and threshold energies. It should be also noted that the determination of effective cross section, when the cross section curve is not a simple step function, requires knowledge of the energy distribution of the particles inducing the nuclear reactions. An unfolding procedure which properly takes into account the whole energy dependence of the cross sections is used later in this chapter.

It is also noticed that the deviations from expected behaviour of particle fluences are most significant for reactions producing ^{61}Cu and ^{7}Be. This can be explained by the fact that the calculated cross sections should not be used for these extreme cases. In particular, ^{7}Be is probably produced mostly as fragments of the spallation reaction rather than as the final reaction product.

The measurement of radioactivity induced by particles provides information of their flux. The study of several activation reactions with different known energy-dependent cross sections enables us to obtain information of their energy distribution. Specifically, in activation detector spectroscopy we search for a solution for an energy spectrum $\varphi(E)$ from a set of activation equations of the form

$$A_j = c_j \int_{E_{min}}^{E_{max}} \sigma_j(E)\, \varphi\, dE, \quad \text{for } j = 1,\ldots,m, \quad (2)$$

the terms of which have been defined in section 2.1.

Equation (2) is a degenerate case of a Fredholm integral equation of the first kind. The mathematical problems associated with the solution, the requirements for a suitable solution method for the particular case of neutron spectroscopy, and the available solution methods have been discussed earlier in detail[12]. A mathematical unfolding method designed to meet all the requirements of a solution procedure has been developed and been incorporated into a Fortran program LOUHI[3]. We use this program to determine the energy spectrum of the particles inducing the measured spallation reactions. For clarity a brief description of the solution method is given below.

The integral equation

$$\int_{E_{min}}^{E_{max}} K(E', E)\, \varphi(E)\, dE = A(E') + \quad (E') \qquad (3)$$

where $K(E',E)$ is the kernel composed of the cross sections, $\varphi(E)$ is the energy spectrum to be determined, $A(E')$ is the normalized vector containing the measured activities, and $\epsilon(E')$ reflects the uncertainties of the cross sections and the measurement errors, is first replaced by a quadrature form

$$K \phi = A + \epsilon \quad . \tag{4}$$

Here A is the measured vector with components A_j and errors ϵ_j, $j = 1,\ldots,m$, ϕ is the solution vector with components ϕ_i, $i = 1,\ldots,n$, and K is the response matrix of dimensions n x m. In the derivation of the quadrature form the solution is approximated by a piecewise linear continuous function. With an adequate number of steps this approximation provides an arbitrary closeness to any real continuous function without prescribing the shape of the solution.

$$Q = Q_o + \gamma (W_1 Q_1 + W_2 Q_2) \tag{5}$$

where

$$Q_o = \sum_{j=1}^{m} r_j^{\epsilon} \epsilon_j^2 = \sum_{j=1}^{m} \left(\frac{A_j^{meas} - A_j^{comp}}{A_j^{meas}} \right)^2 , \tag{5a}$$

$$Q_1 = \sum_{i=1}^{n} r_i^{\phi} (\log \phi_i - \log \phi_i^{o})^2, \quad r_i^{\phi} = \frac{1}{n} , \tag{5b}$$

$$Q_2 = \sum_{i=2}^{n-1} r_i^{d} (\log \phi_{i-1} - 2 \log \phi_i + \log \phi_{i+1})^2, \quad r_i^{d} = \frac{1}{n} . \tag{5c}$$

The term Q_o is related to matching the responses, which in this case are weighted as indicated by the righthand side of the equation (5a). The term Q_1 requires a closeness to a given approximate solution ϕ^o, in this case on a logarithmic scale. The term Q_2 imposes a smoothness requirement by including the numerical second difference of the solution in the sum to be minimized. This condition is also expressed on a logarithmic scale and weighted as indicated in equation (5c). The auxiliary conditions included in terms Q_1 and Q_2 are weighted relatively by W_1 and W_2, and finally γ specifies the overall importance of the prior conditions. In the subsequent computations we do not use any information of an approximate solution, that is W_1 is set to zero.

The minimization is performed in a nonnegative subspace with respect to the parameters ϕ_i defining the solution vector by using a gradient algorith with variable metric[13].

The kernel needed in the computation is obtained by computing the cross sections by using Rudstam's formula as described in section 2.2. The input responses as summarized by the saturation activities in table 6 were used for A vector. When performing the computation with all measured activities some difficulties were encountered. No solution spectrum which would match all the measured responses within even 50 % could be found. This is probably caused by fairly large errors in some of the cross sections, which can be assumed to be accurate only within a factor of two. The elimination of the activities with largest discrepancies between the measured and computed responses enables us to determine a spectrum which matches rather well the remaining activities. These matches as well as the corresponding results of the reactions not included in the solution procedure (simply by setting r_j^{ϵ} equal to zero for those responses) are also summarized in table 6. Figure 6 shows the computed energy spectrum. The energy distribution obtained is in good agreement with other measurements with activation detectors close to loss points[2] as well as with the results of Monte Carlo calculations of the nucleon-meson cascades[9].

When using spallation reactions only, the low energy part of the spectrum is not well defined. This can be explained by the fact that, because of the high thresholds of the cross sections, the principal contribution to the activities comes from the high-energy part of the spectrum and thus the shape of the low-energy part of the spectrum makes little diference in the computed activities.

The difficulties in obtaining a solution spectrum which would match the measured saturation activities of all the reactions points out to the need of checking the computed cross sections against experimental data. The experimental data available is, however, limited and does not cover the entire energy range of interest. The counting methods used in the analysis of induced

activities are equally applicable to cross section measurements and could provide much more information with less experimental effort than the radiochemical techniques previously used for the cross section measurements.

4.3 Results with phosphate glass dosimeters

More than twenty phosphate glass dosimeters were employed in each run. In the earlier report we have discussed the dose distributions measured with these detectors as well as the dependence of the readings on the primary proton energy, target materials, and local shielding. The phosphate glass dosimeters serve also as the reference dosimeter for an intercomparison of more than 20 different directly reading dosimeter types. For a detailed discussion of these results the reader is referred to the earlier report[1].

Here we use the results of the phosphate glass dosimeters to determine practical fluence-to-dose conversion factors for activation detectors, see section 5. For completeness, all readings from these detectors are summarized in table 7.

5. FLUENCE-TO-DOSE CONVERSIONS

Ideally radiation fluences should be converted into doses by integrating their energy distributions multiplied by the corresponding energy dependent conversion factors. In order to obtain the total dose such a procedure should include all types of radiations contributing to the dose.

Activation detectors generally respond to only part of the radiation field, that is to strongly interacting particles. Only in some situations is it thus possible to obtain an accurate dose by using the above procedure with spectra unfolded from activation measurements. In particular, outside a thick shield neutrons often are the principal contributors to the dose and thus the conversion of their fluence yields a good approximation of the dose[2]. Inside the shield, close to a radiation source, a significant fraction of the dose is due to electromagnetic radiation not accounted for by the

activation detectors. Also, when using a small number of detectors it is difficult to determine the energy distribution of the particles. In these cases the fluence-to-dose conversion needs to be done by using direct conversion factors. The simpler conversion is also better suited for practical measurements when large numbers of activation detectors are used in routine measurements. For a constant radiation spectrum there is a constant proportionality, that is a conversion factor, between the fluence and the dose. In order to account for changes in the spectral composition of the field several different fluences, F_j, and conversion factors, d_j, can be used. The dose is then expressed as

$$D = \sum_{j=1}^{ndet} d_j F_j \qquad (6)$$

Several ways can be used for the optimal determination of the conversion factors d_j. Such factors have been calculated for a number of two-detector combinations for determining the dose equivalent by considering a number of representative spectra[14]. For any spectrum the exact conversion is represented by two values which are linearly related. The optimal values for all the spectra are given by a point closest to different straight lines describing the linear relationships. In this approach the conversion factors are determined mathematically without any use of experimental data.

An empirical conversion between the dose to organic materials and the fluences from a two-detector set has been proposed as

$$D\left[\text{rad}\right] = 2\left(2.8 \times 10^{-8} F(^{22}\text{Na})\left[\text{cm}^{-2}\right] + 4.0\times10^{-9} F(^{32}\text{P})\left[\text{cm}^{-2}\right]\right), \qquad (7)$$

where $F(^{22}\text{Na})$ is the high-energy particle fluence above 25 MeV determined by the production of ^{22}Na in aluminum (or by $^{12}\text{C}(n,2n)^{11}\text{C}$ reaction with a 20 MeV threshold) and $F(^{32}\text{P})$ is the fast neutron fluence between approximately 3 and 25 MeV as measured by $^{32}\text{S}(n,p)^{32}\text{P}$ activation reaction[15]. These conversion factors have been obtained by using the fluence-to-dose conversion for tissue-equivalent material and empirical experience. The factor of 2.8×10^{-8} rad cm^2 corresponds to the energy given off by a minimum ionizing particle, electrons of 1 MeV and protons of a few GeV. The conversion factor for a surface

dose from protons to organic material varies from 6×10^{-8} to 3.6×10^{-8} rad cm^2. Charged high energy particles streaming out of the vacuum chamber of a multi-GeV proton accelerator possess energies in the GeV-region and downwards. So an average factor of about 5×10^{-8} rad cm^2 could be used rather than 2.8×10^{-8} rad cm^2. The factor for fast neutrons, 4×10^{-2} rad cm^2, corresponds to the energy dose of neutrons of about 2 MeV. The cross section curves of the reactions $^{27}Al(n,\alpha)^{24}Na$ and $^{32}S(n,p)^{32}P$ peak at about 10 MeV where a conversion value of 7×10^{-9} rad cm^2 is found. Even with this value the contribution by fast neutrons to the total dose still remains rather small.

The multiplying factor 2 in equation (7) approximately accounts for the components in the radiation field which are not detected by the activation detectors. The overall accuracy of this conversion is within a factor of three at locations close to beam loss points.

The conversion factors can also be determined directly by using experimental data. In the following we discuss factors obtained by comparing the doses measured with phosphate glasses to the fluences determined with activation detectors under different experimental conditions.

The optimal conversion factors are determined by minimizing the sum of squares

$$\chi^2 = \sum_{i=1}^{n} \left(\frac{D_i - \sum_{j=1}^{m} d_j F_{ij}}{D_i} \right)^2 \qquad (8)$$

where D_i is the dose measured with a phosphate glass and F_{ij} are the particle fluences measured with activation detectors in the same location. The number of activation detectors is given by m and the number of locations by n. The sum is minimized with respect to the conversion factors d_j.

It should be noted that here we are searching for the best conversion factors corresponding to a representative set of operating parameters and local conditions. The accuracy of the fluence-to-dose conversion should not be expected to be as good as what one can obtain

through the determination of the particle spectrum[2]. Large deviations in the operating conditions are not accounted for by these practical conversion factors and thus they should be applied to similar radiation fields only.

It should be also noted that the resulting conversion factors correspond directly to the doses measured with phosphate glass dosimeters. No additional corrective factor is used to take into account the components of the radiation field which are not detected by the activation detectors.

Conversion factors calculated for different pairs of activation detectors responding to fast neutrons and the high-energy component of the radiation field are given in table 8. Table 9 gives the comparison between the measured doses and those obtained through different conversions. In addition to the ratios between the measured and calculated doses,the table gives the contributions of the high-energy component to the dose.

The new conversion factors indicate a greater contribution to the dose by low-energy and fast neutrons than the coefficients given in equation (7), between 19 and 33 % rather than the average 6 %, respectively. The measured doses are in general higher than those obtained through the equation (7), the mean ratio between the calculated and measured doses is 0.64. The new conversion factors obviously give a better match, since they are determined by matching the measured and calculated doses.

The conversion factors are greater than those which one could obtain from the energy dependent conversion tables in the appropriate energy region. The higher values take into account the components of the radiation field which do not give rise to any response in the activation detectors.

Some comments on the values obtained can be made. The conversion factor for the Al-^{22}Na detector is about twice as much as that for the carbon detector. This is in agreement with the larger fluences measured with the carbon detector with 20 MeV threshold

than with the 30 MeV threshold aluminum detector. The fast neutron reactions $^{27}Al\ (n, \alpha)^{24}Na$ and $^{32}S(n,p)^{32}P$ have about the same thresholds but due to the decrease in the cross section of the latter at neutron energies above 12 MeV a higher conversion factor is found.

The conversion factors computed for the third pair of activation detectors, that is $Al \rightarrow {}^{24}Na$ and $Al \rightarrow {}^{22}Na$, can be modified slightly in opposite directions without making a large difference in the dose calculations. Thus we could use the value 6.0×10^{-8} for the former and 5.0×10^{-8} for the latter reaction. With this modification the conversion factors remain unchanged for each detector for the pairs considered. We can thus summarize the recommended values as follows: 8.5×10^{-9} rad/n/cm^2 for indium detector, 6.0×10^{-8} for $Al \rightarrow {}^{24}Na$, 6.0×10^{-8} for sulphur, 3.0×10^{-8} for carbon, and 5.0×10^{-8} for $Al \rightarrow {}^{22}Na$. These values should be used with fluences calculated by using cross sections given in table 1.

As pointed out earlier the conversion factors determined in this fashion are applicable only to experimental conditions similar to those in our measurements. The doses inside the accelerator tunnel at proton energies between 12 and 24 GeV can be estimated within a factor of two by using these practical fluence-to-dose conversion factors.

6. CONCLUSIONS

The results obtained in this series of experiments at the CERN Proton Synchrotron give us a picture of the radiation distribution at large angles downstream from thick internal targets and of the effect of local shield on it.

The dependence of particle fluxes measured with different activation detectors on the energy of the primary beam was found to be in agreement with our earlier results based on a large number of dosimeter readings[1]. The local shield of up to 40 cm of concrete causes a significant build-up of low-energy particle fluxes and does not reduce the high-energy fluxes or dose levels. It does not provide protection for the components which have to be placed close to loss points.

Similarily, behind some thickness of moderating matter, the low-energy neutron component of the radiation field can rise to such high levels that they contribute significantly to the absorbed dose. For example, the glass enforcement used in magnet coil insulators in high-energy accelerators contains up to 8 % boron oxide. Boron has a very high cross section for the capture of thermal neutrons (755 barn) and the resulting reaction yields a 2.75 MeV α particle which is completely stopped in the insulating material. The thermal neutron flux of 10^8 n/cm^2 per 10^{12} acclerated protons contributes to a yearly dose of about 2×10^7 rad, considering 2000 hours of targetting per year. The dose contribution of these low-energy particles in magnet insulations can thus be as high as 20 %.

The results obtained with spallation detectors show the applicability of high-resolution gamma spectroscopy in identifying and measuring up to 25-30 radioisotopes produced in copper foils. This technique offers the possibility to measure a large number of threshold reactions simultaneously. The limited sensitivity of these detectors restricts their application to areas of high fluxes. The mathematical unfolding of the energy spectrum of the particles inducing the spallation reactions indicates some inconsistencies in the computed cross sections, however, it is possible to determine energy spectra which are in good agreement with our previous understanding of the radiation fields close to loss points.

The intercomparison of the dose and fluence measurements yields a set of practical fluence-to-dose conversion factors applicable to pairs of commonly used activation detectors with different half lives. The dose measurement can thus benefit from the wide measuring ranges attainable with activation detectors and also from the information which they contain about the composition of the radiation field.

ACKNOWLEDGEMENTS

The interest and comments by L. Resegotti and K. Goebel and the cooperation of A.Kjelberg and B.Erdal in making a high-resolution gamma spectrometer available are gratefully acknowledged.

REFERENCES

1) J.T. Routti and M. H. Van de Voorde, Dose measurements near internal targets at the CERN proton synchrotron with intercomparison of different dosimeters, CERN ISR-MA/70-50, October 1970.

2) W.S. Gilbert et al., 1966 CERN-LRL-RHEL shielding experiment at the CERN proton synchrotron, UCRL-17941, Sept. 1968.

3) J.T. Routti, High-energy neutron spectroscopy with activation detectors, incorporating new methods for the analysis of Ge(Li) gamma-ray spectra and the solution of Fredholm integral equations (Ph.D. thesis), UCRL-18514, April 1969.

4) G. Rudstam, Systematics of spallation yields, Zeitschrift für Naturforschung, 21a, 1027, 1966.

5) J.T. Routti and S.G. Prussin, Photopeak method for computer analysis of gamma-ray spectra from semiconductor detectors, Nucl. Instr. Meth., 72, 125, 1969.

6) J.T. Routti, SAMPO, A Fortran program for computer analysis of gamma spectra from Ge(Li) detectors, and other spectra with peaks, UCRL-19452, October 1969.

7) J.H.B. Madsen and M. Van de Voorde, Megarad dosimetry techniques used at the CERN proton synchrotron, Nucl. Instr. Meth., 63, 274, 1968.

8) S. Charalambus, K. Goebel, and D. Nachtigall, Angular distribution of secondary particles and dose-rates produced by 19.2 GeV/c protons bombarding thin Be, Al, Cu, and U targets, CERN report DI/HP/97, Aug. 1967.

9) K. Goebel and J. Ranft, Radiation measurements around a beam stopper irradiated by 19.2 GeV/c protons, and neutron energy spectra from Monte Carlo nucleon-meson cascade calculations, CERN 70-16, May 1970.

10) C.M. Lederer, J.M. Hollander and I. Perlman, Table of isotopes, Sixth edition, John Wiley & Sons, New York, 1968.

11) A.R. Smith, University of California Lawrence Radiation Laboratory, Berkeley, California, private communication, 1970.

12) J.T. Routti, Mathematical considerations of determining neutron spectra form activation measurements, Second International Conference on Accelerator Dosimetry and Experience, Stanford, California, November 1969, USAEC report CONF-691101.

13) W.C. Davidon, Variable metric method for minimization, Argonne National Laboratory report ANL-5990, November 1959.

14) K.B. Shaw, G.R. Stevenson, and R.H. Thomas, Evaluation of dose equivalent from neutron energy spectra, Health Physics 17, 459, 1969.

15) K. Goebel and M. Nielsen, Routine flux and dose-rate measurements near the PS vaccuum chamber, CERN internal report HP-69-69, February 1969.

TABLE 1

Characteristics of conventional activation detectors

Detector	Size	Principal sensitivity	Nuclear reaction	Cross section used	Induced radioactivity	Half life	Counting
Indium foil	50 mm Ø	Thermal neutrons	$^{115}In(n,\gamma)^{116m}In$	Direct calibration	β^-; γ: 0,47 MeV(36%) 1.09 MeV(53%) 1.29 MeV(80%)	54 min	Proportional counter
Cd-covered In foil	-"-	Epicadmium neutrons	- " -	- " -	- " -	- " -	- " -
Moderated In foil	50 mm Ø in 12 cm Cd-covered moderator	0.02-20 MeV neutrons	- " -	- " -	- " -	- " -	- " -
Sulphur pellet	10 mm Ø x 5 mm	3-25 MeV neutrons	$^{32}S(n,p)^{32}P$	300 mbarn		14.0 d	- " -
Al→^{24}Na	50 mm Ø x 0.1 mm	6-25 MeV neutrons	$^{27}Al(n,\alpha)^{24}Na$	120 mbarn	β^-; γ: 1.37 MeV(100%) 2.75 MeV(100%)	15.0 h	- " -
Carbon Scintillator	50 mm Ø x 50 mm	Hadrons above ~20 MeV	$^{12}C(n,2n)^{11}C$ $^{12}C(p,np)^{11}C$	22 mbarn	β^+: (100%)	20.3 min	Scintillation counting
Al→^{22}Na	50 mm Ø x 0.1 mm	Hadrons above ~25 MeV	$^{27}Al(spall)^{22}Na$	20 mbarn	β^+: (90%) γ : 1,275(100%)	2.6 y	Proportional counter

TABLE 2

Beam and target conditions

Run	Target	Momentum (GeV/c)	Shielding	Protons per pulse	Date
1	Be	24	None	1.06×10^{12}	7.3.1970
2	Be	19.2	None	1.04×10^{12}	7.3.1970
3	Cu	24	None	1.17×10^{12}	19.3.1970
4	Be	12	None	1.01×10^{12}	19.3.1970
5	Be	12	Concrete	1.14×10^{12}	10.4.1970
6	Be	24	Concrete	1.19×10^{12}	10.4.1970

TABLE 3

Fluences measured with activation detectors normalized to 10^{12} accelerated protons

Experiment			1	2	3	4	5	6
Momentum (GeV/c)			24	19,2	24	12	12	24
Target			Be	Be	Cu	Be	Be	Be
Shielding			None	None	None	None	Concrete	Concrete
Detector	Position	Units	Fluences					
Thermal	104	$x10^{6}$	8.51	6.34	7.91	6.65	15.2	41.6
In foil	204		9.00	7.00	2.41	3.64	35.8	112.7
	304		10.9	8.19	4.92	1.57	38.1	78.4
Epicadmium	104	$x10^{7}$	0.73	0.50	1.40	0.66	1.83	1.69
In foil	204		1.97	1.47	2.66	1.01	4.55	4.37
	304		1.99	1.20	1.68	2.23	3.53	5.25
Moderated	104	10^{8}	2.43	2.16	3.34	1.25	2.07	3.72
In foil	204		2.77	2.63	3.25	1.39	4.26	8.94
	304		4.57	4.13	4.46	2.01	4.14	9.53
Sulphur	104	$x10^{7}$	5.69	5.97	8.52	3.08	4.74	8.08
	204		6.66	6.82	6.95	3.21	6.67	12.4
	304		8.22	8.19	7.26	3.69	6.13	12.7
$Al \rightarrow {}^{24}Na$	104	$x10^{7}$	7.69	5.06	2.98	1.14	4.26	6.85
	204		9.00	6.85	2.58	1.26	5.27	9.24
	304		9.95	7.27	2.31	1.24	4.64	9.71
Carbon	104	$x10^{8}$	2.84	3.40	3.60	1.66	1.89	2.22
	204		3.79	4.48	5.49	1.55	2.02	2.22
	304		4.18	4.01	4.81	1.56	2.47	4.54
$Al \rightarrow {}^{22}Na$	104	$x10^{8}$	1.38	1.68	2.51	0.92	1.04	1.75
	204		1.97	2.06	2.62	1.20	1.09	2.30
	304		2.00	2.24	2.32	1.17	1.01	1.63

TABLE 4

Correlations between measured fluences

Experiments	2/1	4/1	5/6	3/1	5/4	6/1
Variable param.	19.2/24GeV/c	12/24GeV/c	12/24GeV/c	Cu/Be target	Concr./Air	Concr./Air
Constant param.	Be target No shield	Be target No shield	Be target Concrete	24 GeV/c No shield	Be target 12 GeV/c	Be target 24 GeV/c
Detector						
Thermal	0.76	0.42	0.38	0.53	7.51	8.19
Epicadmium	0.68	0.83	0.88	1.22	2.54	2.41
Moderated	0.91	0.48	0.47	1.13	2.25	2.27
Sulphur	1.02	0.49	0.53	1.10	1.76	1.61
$Al \rightarrow {}^{24}Na$	0.72	0.14	0.55	0.30	3.89	0.97
Carbon	1.10	0.44	0.71	1.29	1.34	0.83
$Al \rightarrow {}^{22}Na$	1.11	0.62	0.55	1.39	0.95	1.06
All above	0.90	0.49	0.58	1.00	2.89	2.47
Phosphate glass	0.81	0.69	0.84	1.01	1.10	0.92

TABLE 5

Analysis of gamma-ray spectra of Cu foil counted after 11 hours (1) and 51 hours (2)

Radio-isotope	Half-life	Spectrum	Measured energy (keV)	Energy difference (keV)	Photopeak area (counts)	Reference relative intensity (%)	Measured relative intensity *) % normalised	Saturation activity (d/min)	Inter-fering isotopes
^{61}Cu	3.3 h	1	282.7	-1.3	1.65×10^4	12.0	12.0*	2.91×10^3	
		1	588.6	0.6	4.33×10^2	1.5	0.7	1.41×10^3	
		1	655.8	0.8	4.80×10^3	11.0	9.4	2.49×10^3	
		1	907.9	1.9	3.09×10^2	1.5	0.8	1.51×10^3	
^{65}Ni	2.56h	1	1 115.2	0.2	3.30×10^2	16.0	20.3	2.65×10^2	
		1	1 481.7	0.7	2.87×10^2	25.0	25.0	2.09×10^2	
^{57}Ni	36.0 h	1	1 377.4	-0.2	4.14×10^2	84.9	84.9*	1.06×10^2	
		2	127.0	-0.3	7.87×10^3	15.0	16.8	1.34×10^2	
		2	1 377.5	-0.1	2.99×10^3	84.9	84.9*	1.21×10^2	
		2	1 757.4	-0.2	1.79×10^2	6.3	6.8	1.30×10^2	
		2	1 919.4	-0.1	4.16×10^2	14.9	15.9	1.29×10^2	
^{60}Co	5.26y	2	1 172.9	-0.3	6.57×10^2	100.0	100.0*	8.77×10^3	
		2	1 333.0	0.5	1.23×10^3	100.0	100.0	1.93×10^4	^{52}Mn
^{58}Co	71.3 d	1	810.0	-0.5	1.42×10^3	98.0	98.0*	7.07×10^3	
		2	810.0	-0.5	3.03×10^4	98.0	98.0*	1.10×10^4	
^{57}Co	270. d	2	122.0	-0.1	3.14×10^4	85.3	85.3*	6.08×10^3	
		2	136.2	-0.2	4.53×10^3	8.4	19.3	1.04×10^4	

TABLE 5 (cont'd)

Radio-isotope	Half-life	Spectrum	Measured energy (keV)	Energy difference (keV)	Photopeak area (counts)	Reference relative intensity (%)	Measured relative intensity *) % normalised	Saturation activity (d/min)	Interfering isotopes
^{56}Co	77.3 d	1	846.6	-0.2	1.78×10^3	100.0	100.0*	9.70×10^3	^{56}Mn, ^{52}Mn
		2	846.8	0.1	3.96×10^3	100.0	100.0*	1.56×10^3	^{52}Mn
		2	1 037.1	-0.8	2.03×10^3	13.2	62.0	7.35×10^3	
		2	1 238.1	-0.2	1.69×10^3	69.4	64.0	1.44×10^3	
		2	1 771.1	-0.4	2.37×10^2	15.3	13.8	1.41×10^3	
		2	2 035.1	0.1	1.09×10^2	7.3	6.7	1.43×10^3	
^{55}Co	18.2 h	1	930.9	0.9	1.06×10^3	80.0	80.0*	1.08×10^2	
		1	983.0	-2.0	5.84×10^2	0.9	47.0	5.65×10^3	^{48}V, ^{55}Co
		1	1 368.6	-1.4	3.12×10^2	4.2	37.5	9.68×10^2	^{24}Na
		1	1 408.5	-1.5	1.26×10^2	13.0	15.7	1.31×10^2	^{45} Ti
		2	930.0	0.9	3.43×10^3	80.0	80.0*	1.20×10^2	
		2	1 367.2	-1.4	7.84×10^2	4.2	28.7	8.30×10^2	^{24}Na
		2	1 410.0	-1.6	5.03×10^2	13.0	19.1	1.78×10^2	^{45}Ti
^{59}Fe	45.6 d	2	1 099.1	-0.2	1.42×10^3	56.2	56.2*	7.75×10^2	
		2	1 291.4	0.9	8.64×10^2	43.5	41.5	7.42×10^2	
^{56}Mn	2.58h	1	846.6	0.0	1.78×10^3	99.0	99.0*	1.74×10^2	^{52}Mn, ^{56}Co
		1	1 810.7	-0.5	1.97×10^2	30.0	25.1	1.43×10^2	
^{54}Mn	303. d	2	843.8	0.0	2.07×10^3	100.0	100.0*	3.15×10^3	
^{52}Mn	5.6 d	1	744.0	0.0	1.53×10^3	82.0	82.8	6.95×10^2	
		1	846.6	-0.4	1.78×10^3	2.6	107.2	2.83×10^4	56Co, ^{56}Mn
		1	935.1	0.1	1.24×10^3	84.0	79.7	6.52×10^2	
		1	1 434.0	0.0	9.27×10^2	100.0	100.0*	6.88×10^2	
		2	744.0	0.0	2.00×10^4	82.0	92.1	8.05×10^2	

TABLE 5 (cont'd)

Radio-isotope	Half-life	Spectrum	Measured energy (keV)	Energy difference (keV)	Photopeak area (counts)	Reference relative intensity (%)	Measured relative intensity *) % normalised	Saturation activity (d/min)	Interfering isotopes
		2	846.8	-0.2	3.96×10^3	2.6	20.1	5.56×10^3	^{56}Co, ^{56}Mn
		2	935.2	0.2	1.66×10^4	84.0	89.6	7.69×10^2	
		2	1 246.1	0.1	6.29×10^2	6.0	4.8	5.76×10^2	
		2	1.333.0	1.0	1.23×10^3	6.0	10.4	1.23×10^3	
		2	1 434.0	0.0	1.10×10^4	100.0	100.0*	7.17×10^2	
		2	1 731.8	1.8	1.41×10^2	0.05	1.6	2.31×10^4	
^{51}Cr	27.8 d	2	319.6	-0.5	4.94×10^3	9.8	9.8*	2.63×10^3	
^{48}Cr	23.0 h	2	308.2	-1.8	1.98×10^3	99.0	99.0*	1.51×10^1	
^{48}V	16.0 d	1	983.0	-0.3	5.84×10^2	100.0	100.0*	7.58×10^2	^{48}Sc, ^{55}Co
		2	943.6	-1.4	5.36×10^2	10.0	6.3	5.10×10^2	
		2	983.0	-0.3	8.21×10^3	100.0	100.0*	8.20×10^2	^{48}Sc, ^{55}Co
^{45}Ti	3.08h	1	1 408.5	0.5	1.26×10^2	0.3	0.3*	5.64×10^3	^{55}Co
^{48}Sc	1.83d	1	983.0	-0.3	5.48×10^2	100.0	100.0*	9.91×10^1	^{48}V
		2	983.0	-0.3	8.21×10^3	100.0	100.0*	1.95×10^2	^{48}V
^{47}Sc	3.43d	1	158.9	-1.1	2.81×10^3	73.0	73.0*		
		2	158.9	-1.1	3.44×10^4	73.0	73.0*		
^{46}Sc	83.9 d	2	889.2	0.0	9.18×10^2	100.0	100.0*	3.99×10^2	
		2	1 120.3	-0.2	8.79×10^2	100.0	126.0	5.00×10^2	^{44}Sc

TABLE 5 (cont'd)

Radio-isotope	Half-life	Spectrum	Measured energy (keV)	Energy difference (keV)	Photopeak area (counts)	Reference relative intensity (%)	Measured relative intensity *) % normalised	Saturation activity (d/min)	Inter-fering isotopes
^{44m}Sc	2.44d	1	271.0	-0.2	3.26×10^3	89.0	89.0*	2.01×10^2	
		1	1 156.8	-0.2	1.50×10^3	1.5		2.64×10^4	^{44}Sc
		2	271.0	-0.2	3.71×10^4	89.0	89.0*	2.64×10^2	
		2	1 120.3	0.3	8.79×10^2	1.2		2.17×10^3	^{46}Sc
		2	1 156.8	-0.2	7.65×10^3	1.5		1.57×10^4	^{44}Sc
^{44}Sc	4.0 h	1	1 156.8	-0.2	1.50×10^3	99.0	99.0*	1.29×10^2	
^{43}Sc	3.9 h	1	617.3	-1.7	5.52×10^2	1.0	1.0	2.53×10^3	^{43}K
^{43}K	22.4 h	1	372.6	-0.4	3.17×10^3	85.0	85.0*	1.33×10^2	
		1	588.6	-1.4	4.33×10^2	13.0	20.0	2.03×10^2	^{61}Cu, ^{42}K
		1	617.3	-1.7	5.55×10^2	81.0	27.4	4.46×10^1	^{43}Sc
		2	372.5	-0.5	5.48×10^3	85.0	85.0*	5.83×10^1	
		2	617.3	-1.7	2.56×10^3	81.0	39.6	5.24×10^1	^{43}Sc
^{42}K	12.4 h	1	588.6	1.6	4.33×10^2	0.18	21.9	1.03×10^5	^{61}C , ^{43}K
		1	1 524.6	0.6	1.28×10^2	18.0	18.0*	8.50×10^1	
		2	1 524.5	0.5	2.23×10^2	18.0	18.0*	1.06×10^2	
^{24}Na	15.0 h	1	1 368.6	0.1	3.12×10^2	100.0	100.0*	3.62×10^1	^{55}Co
		2	1 368.6	0.1	7.84×10^2	100.0	100.0*	4.35×10^1	^{55}Co
^{7}Be	53.6 d	2	477.2	-0.3	1.99×10^3	10.3	10.3*	2.77×10^3	

TABLE 6

Results of fluence and spectral determinations with Cu-spallation detectors

Radioisotope measured	Saturation activity $^{d}/(gmin)$	Threshold (MeV)	Cross section (mbarn)	Fluence above threshold ($^{1}/cm^{2}$)	LOUHI match calc./meas. (weight)
^{61}Cu	$2.91x10^{3}$	8	12.6	$4.03x10^{5}$	8.28 (0)
^{60}Co	$8.77x10^{3}$	13	11.2	$1.31x10^{6}$	1.19 (0)
^{59}Fe	$7.75x10^{2}$	18	2.05	$6.97x10^{5}$	1.27 (1)
^{58}Co	$1.10x10^{4}$	23	35.5	$5.33x10^{5}$	1.07 (1)
^{56}Mn	$1.43x10^{2}$	26	4.53	$5.47x10^{4}$	5.28 (0)
^{57}Ni	$1.21x10^{2}$	28	0.94	$2.17x10^{5}$	1.81 (0)
^{57}Co	$6.08x10^{3}$	28	16.8	$6.07x10^{5}$	0.65 (1)
^{55}Co	$1.20x10^{3}$	30	1.18	$1.79x10^{5}$	1.25 (0)
^{56}Co	$1.41x10^{3}$	35	5.2	$4.89x10^{5}$	0.60 (1)
^{54}Mn	$3.15x10^{3}$	50	2.72	$2.03x10^{5}$	8.78 (0)
^{52}Mn	$6.88x10^{2}$	67	7.24	$1.69x10^{5}$	0.74 (1)
^{48}V	$5.10x10^{2}$	72	9.30	$9.86x10^{4}$	0.77 (1)
^{51}Cr	$2.63x10^{3}$	75	21.1	$2.15x10^{5}$	0.50 (0)
^{48}Sc	$9.91x10^{1}$	80	0.58	$3.08x10^{5}$	0.24 (0)
^{46}Sc	$3.99x10^{2}$	85	8.11	$8.87x10^{4}$	0.72 (1)
^{48}Cr	$1.51x10^{1}$	105	0.40	$6.79x10^{4}$	1.12 (1)
^{44m}Sc	$2.64x10^{2}$	160	11.0	$3.96x10^{4}$	1.37 (1)
^{43}K	$5.83x10^{1}$	180	0.95	$1.09x10^{5}$	0.48 (0)
^{42}K	$8.50x10^{1}$	220	3.80	$4.03x10^{4}$	1.19 (0)
^{24}Na	$3.62x10^{1}$	380	2.46	$2.60x10^{4}$	0.98 (1)
^{7}Be	$2.77x10^{3}$	560	0.21	$2.31x10^{7}$	0.00018 (0)

TABLE 7

The phosphate glass dosimeter readings in rad normalized to 10^{12} accelerated protons

Experiment	1	2	3	4	5	6
Momentum (GeV/c)	24	19.2	24	12	12	24
Target	Be	Be	Cu	Be	Be	Be
Shielding	Air	Air	Air	Air	Concr.	Concr.
Position						
101	281.9	334.3	280.8	153.9	251.5	253.0
102	33.9	40.5	65.4	22.6	44.9	58.0
103	20.1	16.0	25.2	15.4	13.2	18.7
104	14.0	11.7	13.6	11.3	10.3	12.8
105	137.7	135.2	119.6	45.2	112.3	141.9
106	29.2	27.9	39.7	17.4	20.6	30.0
107	14.6	12.9	16.0	10.8	11.3	14.7
108	10.8	9.5	10.2			10.3
109	206.6	216.3	314.7	62.6	141.6	219.6
110		51.7	51.8	46.7	27.8	39.8
111	22.8	17.2	21.3	12.1	16.6	16.0
112	12.8	11.9	15.5	10.3	10.7	11.3
113	104.5	116.5	136.5	49.8	66.4	127.7
114	24.8	26.3	35.3	18.3	21.0	28.5
115	14.6	13.4	17.9	10.8	12.2	14.0
116	12.3	11.1	12.6	9.5	10.3	10.8
201	455.2	211.7	117.6	123.1	171.9	447.0
202	91.0	85.1	128.8	33.4	62.5	95.3
203	21.6	19.3	26.1	15.7	16.6	26.5
204	15.2	12.7	16.5	10.8	12.5	15.2
205		155.0	116.2	60.0	96.2	211.2
206	40.3	35.7	33.4	21.0	34.7	69.7
207	21.0	18.7	19.2	13.9	15.4	22.1
208	14.6	12.7	12.1	10.2	11.6	12.8
209	215.9	132.7	290.4	80.0	179.7	257.9

TABLE 8

Conversion factors for dose calculations from measured fluences

Possible application	Fast neutron component		High energy component		Used in the calculation of ... a)
	Reaction	Factor $_2$ rad cm	Reaction	Factor $_2$ rad cm	
Long irradiations b)	$^{32}S(n,p)\ ^{32}P$	4.10^{-9}	$^{27}Al(p,spal)^{22}Na$	$2.8.10^{-8}$	D1
Short irradiation (1 hour)	$^{115}In(n,\gamma)^{116}In$ fast neutrons moderated	$8.5.10^{-9}$	$^{12}C(p,pn)^{11}C$	3.10^{-8}	D2
Short irradiation (1 hour)	$^{27}Al(n,x)^{24}Na$	6.10^{-8}	$^{12}C(p,pn)^{11}C$	3.10^{-8}	D3
Medium long irradiation (hours)	$^{27}Al(n,x)^{24}Na$	$4.7.10^{-8}$	$^{27}Al(p,spal)^{22}Na$	6.10^{-8}	D4
Medium long irradiation (hours) c)	$^{27}Al(n,\alpha)^{24}Na$	6.10^{-8}	$^{27}Al(p,spal)^{22}Na$	5.10^{-8}	D4 *
Long irradiation (days)	$^{32}S(n,p)^{32}P$	6.10^{-8}	$^{27}Al(p,spal)^{22}Na$	5.10^{-8}	D5

a) see table 9

b) Goebel's formula

c) Practical conversion factors

TABLE 9

Comparison of measured and calculated doses

Experiment		1	2	3	4	5	6	Averages
Momentum GeV/c		24	19.2	24	12	12	24	
Target		Be	Be	Cu	Be	Be	Be	
Shield		None	None	None	None	Concrete	Concrete	
	Pos.							
Phosphate-	104	14.0	11.7	13.6	11.3	10.3	12.8	
glass, D_M	204	15.2	12.7	16.5	10.8	12.5	15.2	
	304	17.9	13.7	17.4	10.8	13.2	14.6	
D_1/D_M	104	0.58(0.94)	0.85(0.95)	1.08(0.95)	0.46(0.95)	0.61(0.94)	0.82(0.94)	0.64 ± 0.02
	204	0.76(0.95)	0.95(0.95)	0.93(0.96)	0.65(0.96)	0.53(0.92)	0.91(0.93)	(0.94 ± 0.004)
	304	0.66(0.94)	0.96(0.95)	0.68(0.96)	0.63(0.96)	0.47(0.92)	0.68(0.90)	
D_2/D_M	104	0.75(0.80)	1.02(0.85)	1.00(0.79)	0.53(0.82)	0.72(0.76)	0.76(0.67)	0.90 ± 0.06
	204	0.90(0.83)	1.30(0.86)	1.16(0.85)	0.54(0.79)	0.77(0.62)	0.93(0.46)	(0.75 ± 0.024)
	304	0.91(0.76)	1.13(0.77)	1.04(0.79)	0.59(0.73)	0.82(0.67)	1.44(0.63)	
D_3/D_M	104	0.92(0.65)	1.12(0.77)	0.91(0.86)	0.49(0.88)	0.79(0.69)	0.83(0.62)	0.91 ± 0.06
	204	1.09(0.68)	1.44(0.78)	1.08(0.91)	0.49(0.86)	0.73(0.65)	0.79(0.54)	$(0.75 \pm 0.0\ 6)$
	304	1.02(0.68)	1.18(0.73)	0.89(0.91)	0.50(0.86)	0.76(0.72)	1.28(0.70)	
D_4/D_M	104	0.85(0.70)	1.07(0.81)	1.22(0.92)	0.54(0.91)	0.81(0.76)	1.08(0.77)	0.94 ± 0.05
	204	1.06(0.74)	1.24(0.80)	1.03(0.93)	0.73(0.92)	0.73(0.73)	1.20(0.76)	(0.81 ± 0.021)
	304	0.94(0.72)	1.24(0.80)	0.87(0.93	0.71(0.92)	0.63(0.74)	0.96(0.68)	

TABLE 9 (cont'd)

Experiment		1	2	3	4	5	6	Averages
Momentum GeV/c		24	19.2	24	12	12	24	
Target		Be	Be	Cu	Be	Be	Be	
Shield		None	None	None	None	Concrete	Concrete	
	Pos.							
D_5/D_M	104	0.75(0.67)	1.04(0.70)	1.32(0.71)	0.58(0.72)	0.79(0.65)	1.08(0.64)	0.94±0.05
	204	0.92(0.72)	1.15(0.72)	1.06(0.76)	0.74(0.76)	0.77(0.58)	1.26(0.61)	(0.67±0.016)
	304	0.84(0.67)	1.19(0.70)	0.93(0.73)	0.76(0.73)	0.67(0.58)	1.06(0.52)	
D_4^*/D_M	104	0.82(0.60)	0.98(0.73)	1.06(0.88)	0.47(0.87)	0.76(0.67)	1.01(0.68)	0.86±0.047
	204	1.01(0.65)	1.14(0.71)	0.89(0.89)	0.63(0.89)	0.69(0.63)	1.12(0.67)	(0.73±0.013)
	304	0.89(0.63)	1.14(0.72)	0.75(0.89)	0.61(0.89)	0.59(0.64)	0.93(0.58)	

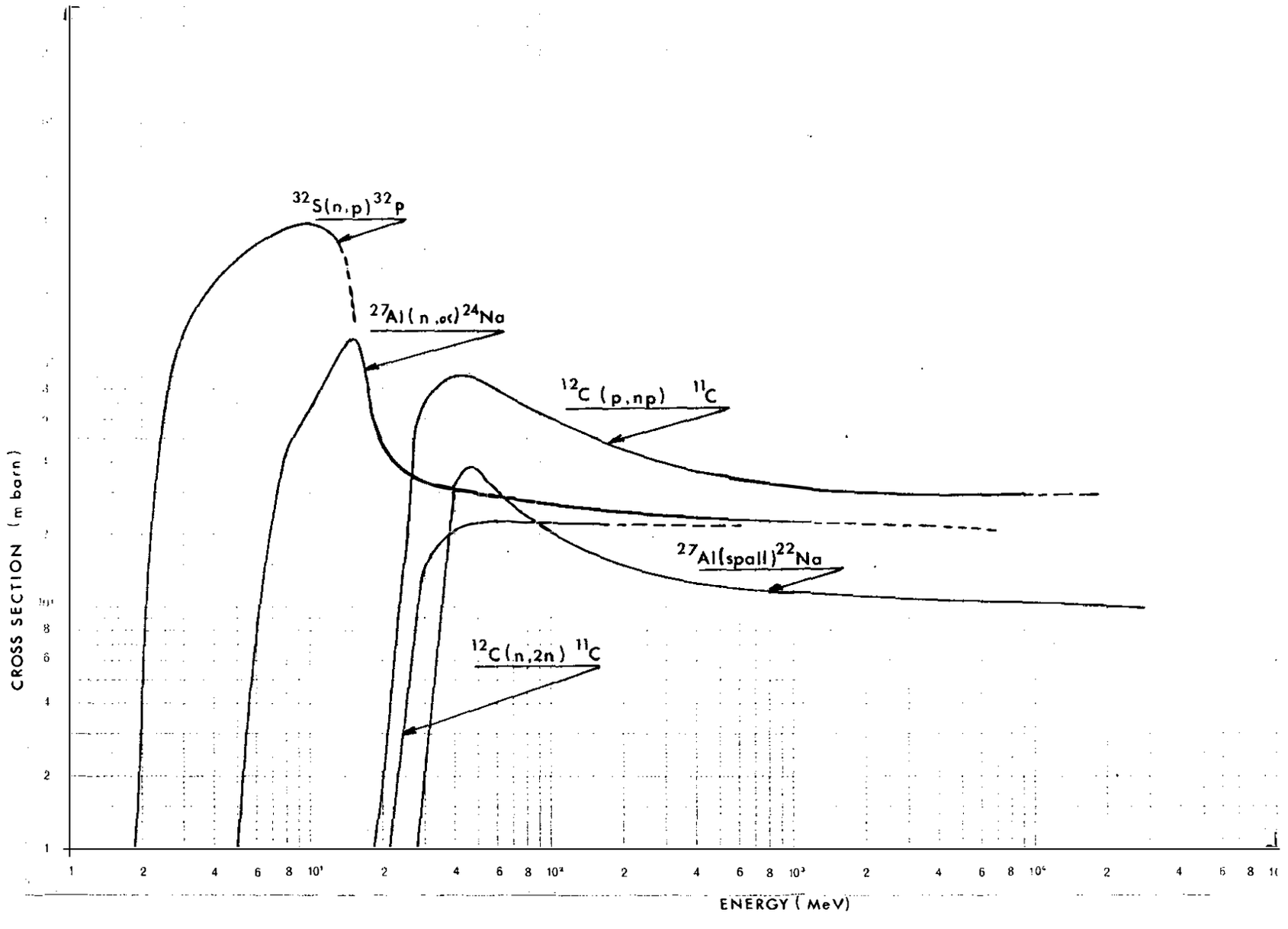

Figure 1. The cross sections of conventional threshold detectors.

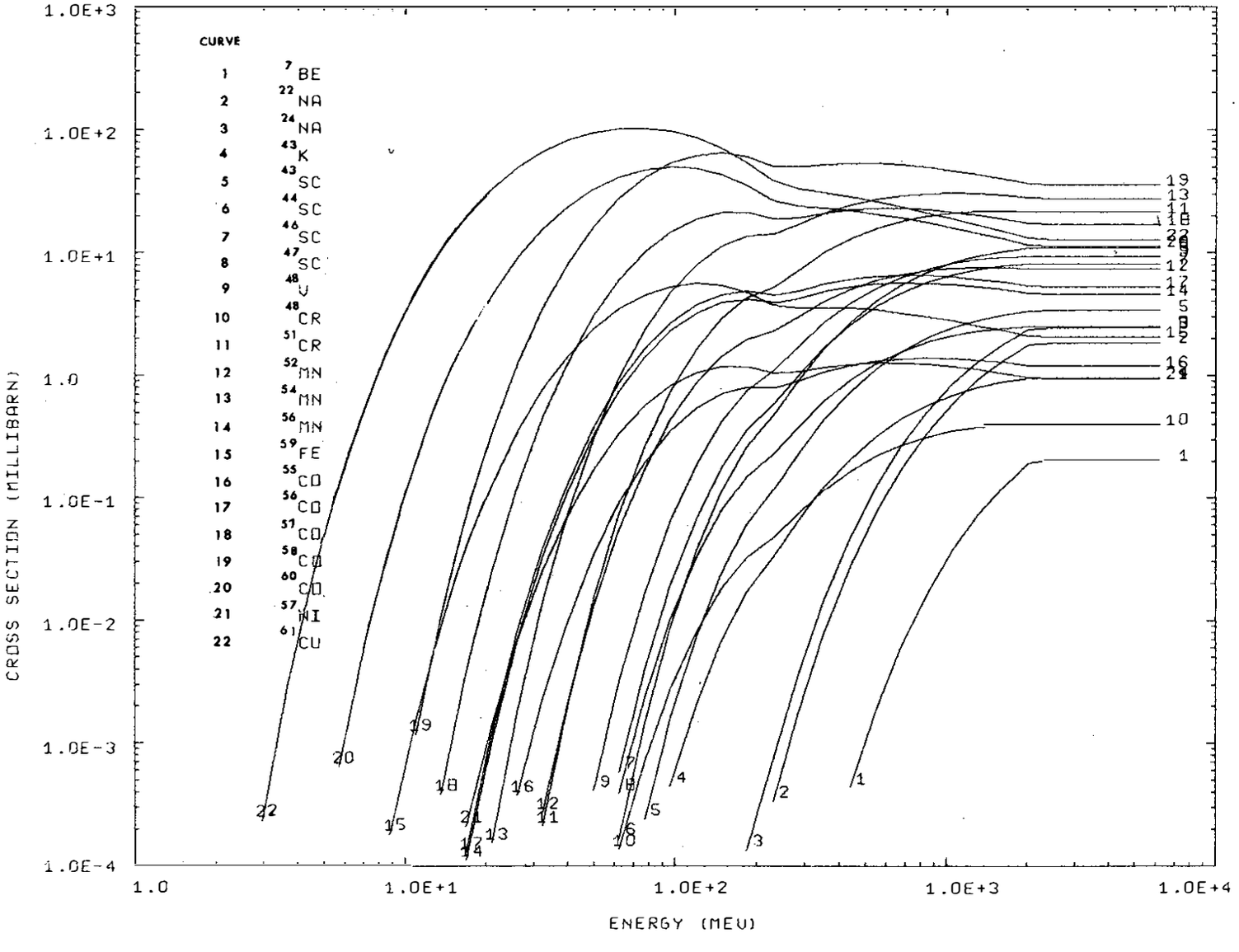

Figure 2. Calculated spallation yields for different reaction products from Cu target.

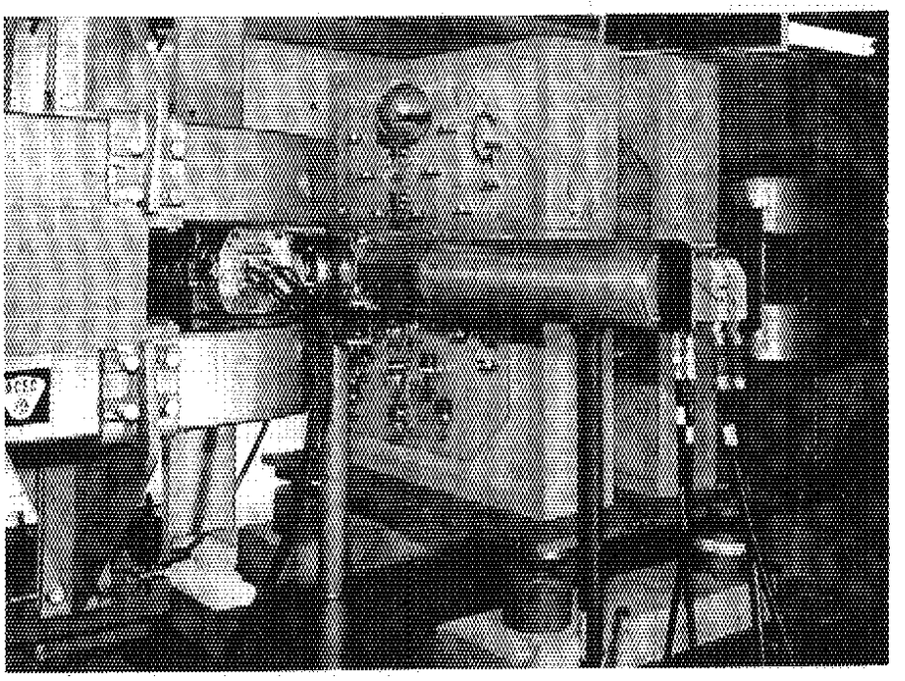

Figure 3. The exposure area at the straight section 47 of the CERN Proton Synchrotron. The dosimeters and activation detectors are placed on three plates downstream from the target box in the foreground. In this run 20 cm thick slabs of concrete are placed between the plates.

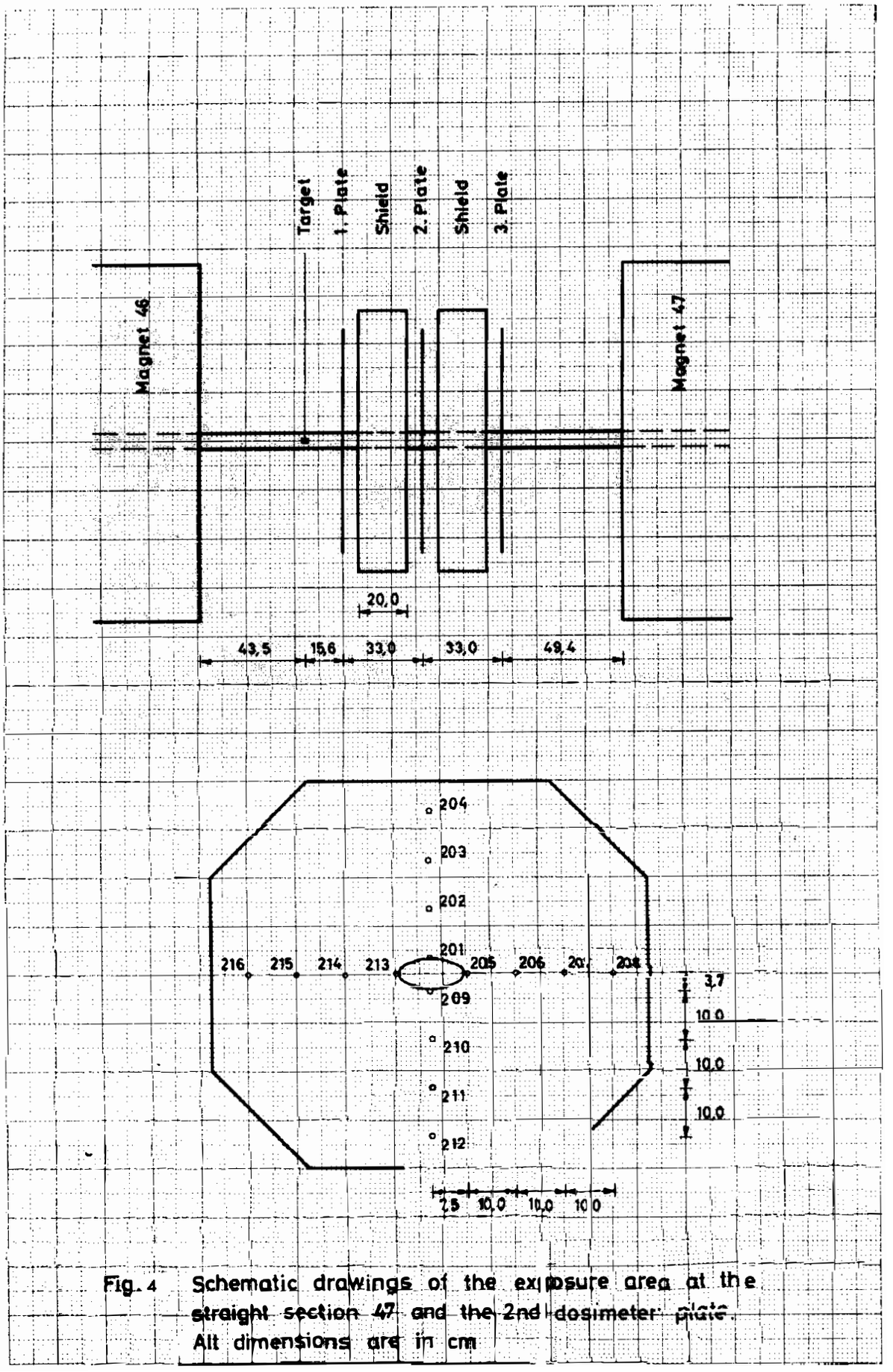

Fig. 4 Schematic drawings of the exposure area at the straight section 47 and the 2nd dosimeter plate. All dimensions are in cm

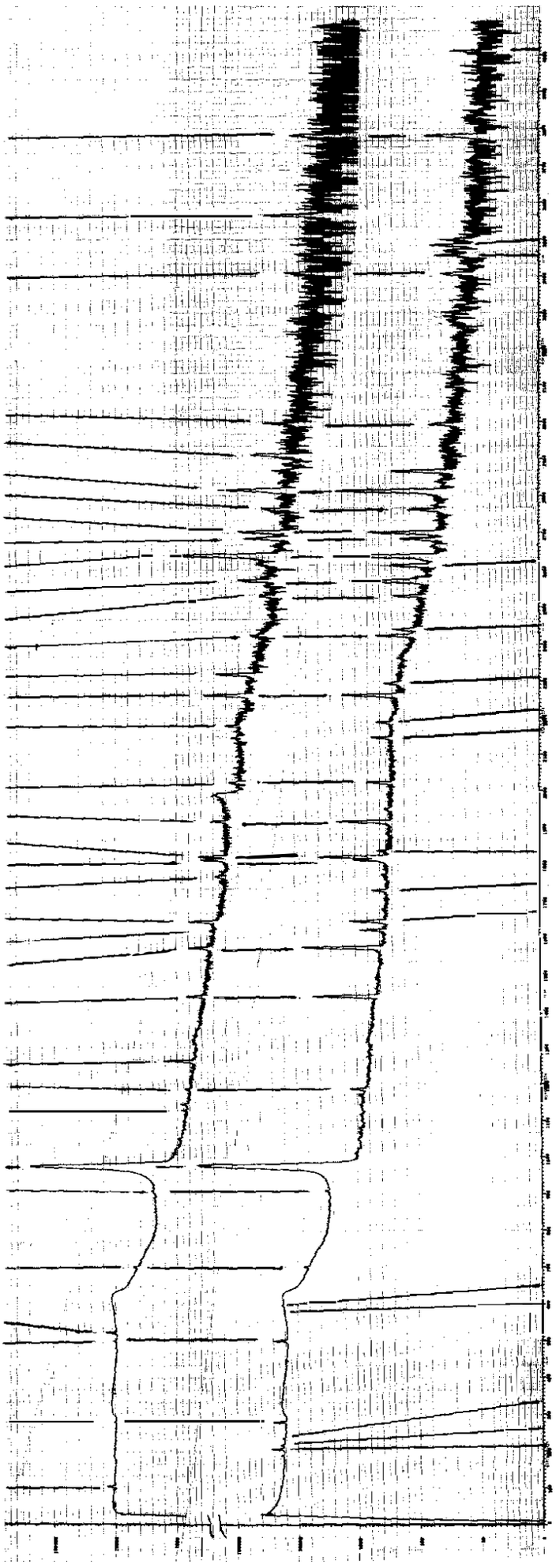

Figure 5. Gamma spectra of Cu-foil after 11 h and 51 h waiting times.

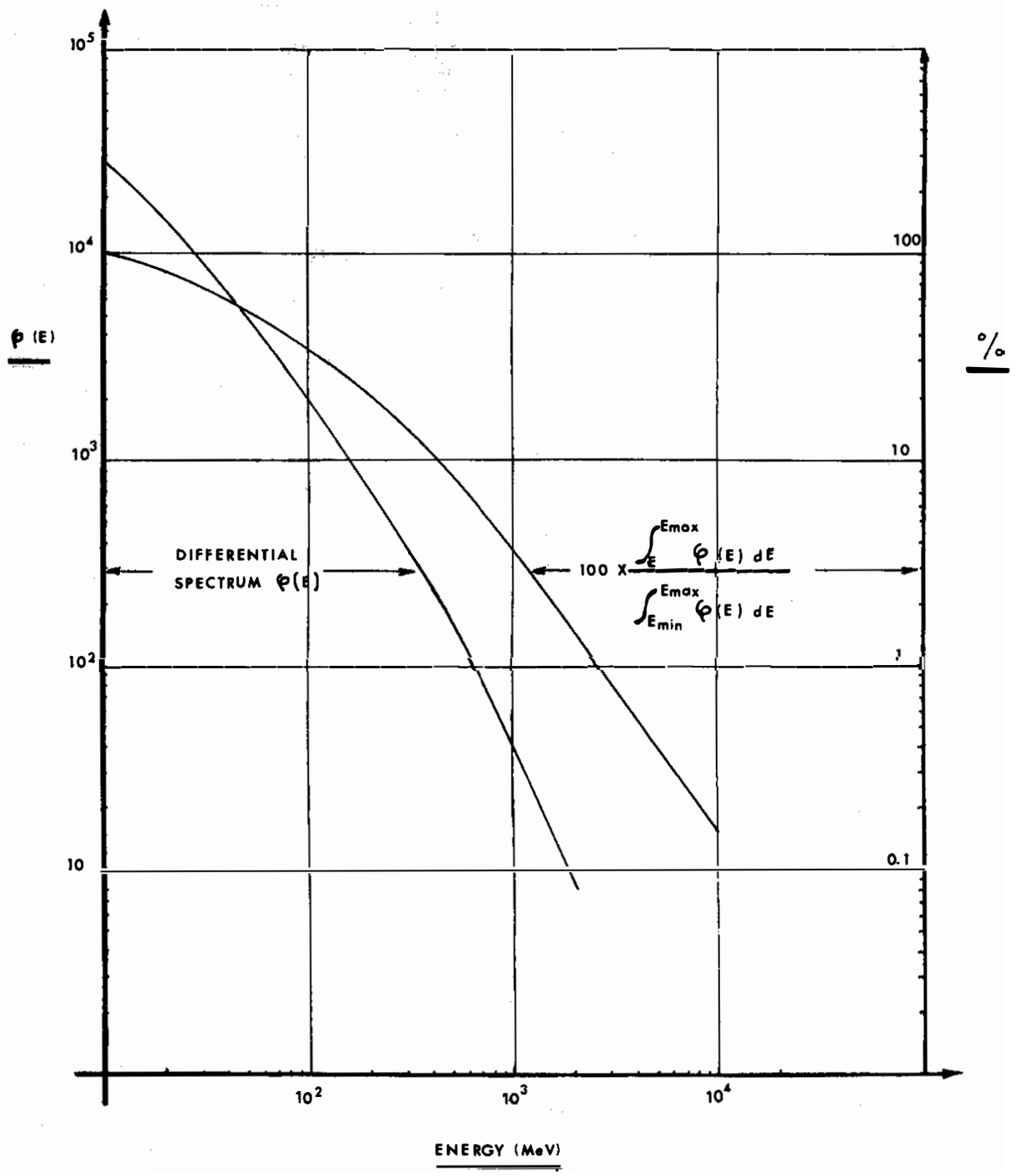

Figure 6. Differential and integral spectra of particles as determined from the measured activities caused by spallation reactions in a Cu detector. The integral spectrum gives the fraction of particles in per cent above any lower limit.